ADVANCED ENERGY MATERIALS
www.advenergymat.de

An Air-Stable and Dendrite-Free Li Anode for Highly Stable All-Solid-State Sulfide-Based Li Batteries

*Jianwen Liang, Xiaona Li, Yang Zhao, Lyudmila V. Goncharova, Weihan Li, Keegan R. Adair, Mohammad Norouzi Banis, Yongfeng Hu, Tsun-Kong Sham, Huan Huang, Li Zhang, Shangqian Zhao, Shigang Lu, Ruying Li, and Xueliang Sun**

Li metal is a promising anode material for all-solid-state batteries, owing to its high specific capacity and low electrochemical potential. However, direct contact of Li metal with most solid-state electrolytes induces severe side reactions that can lead to dendrite formation and short circuits. Moreover, Li metal is unstable when exposed to air, leading to stringent processing requirements. Herein, it is reported that the Li_3PS_4/Li interface in all-solid-state batteries can be stabilized by an air-stable Li_xSiS_y protection layer that is formed in situ on the surface of Li metal through a solution-based method. Highly stable Li cycling for over 2000 h in symmetrical cells and a lifetime of over 100 cycles can be achieved for an all-solid-state $LiCoO_2$/Li_3PS_4/Li cell. Synchrotron-based high energy X-ray photoelectron spectroscopy in-depth analysis demonstrates the distribution of different components within the protection layer. The in situ formation of an electronically insulating Li_xSiS_y protection layer with highly ionic conductivity provides an effective way to prevent Li dendrite formation in high-energy all-solid-state Li metal batteries.

1. Introduction

Li metal is an attractive anode material for all-solid-state lithium batteries (ASSLBs) because of its high specific capacity (3860 mAh g^{-1}) and low electrochemical potential (−3.04 V vs the standard hydrogen electrode).[1–4] Moreover, the use of intrinsically nonflammable inorganic solid-state electrolytes (SSEs) can theoretically solve the safety issue associated with thermal runaway.[3,4] Various SSEs have been recently developed, including oxide-, sulfide-, halide-, and borohydride-based SSEs. Sulfide-based SSEs have emerged as one of the most promising candidates for use in ASSLBs due to their mechanical properties and ultrahigh ionic conductivity which can reach as high as 10^{-2} S cm^{-1} at room temperature.[5–8] However, pure Li metal is still unsuitable for real-application in sulfide-based ASSLBs due to the side reactions at the interface.

Similar to conventional liquid-based lithium ion batteries, the first major obstacle for the use of Li metal anodes is the penetration of Li dendrites through the sulfide-based SSEs, which raises safety concerns and often results in the decay of battery performance or even short circuit.[9,10] Among the typical sulfide-based SSEs, such as $Li_{10}GePS_{12}$,[11,12] Li_3PS_4 (glass or ceramic),[13–17] and Li_6PS_5X (X = Cl, Br, I),[18,19] the formation of lithium dendrites in Li_3PS_4 system is well-recognized.[13–16,20,21] It is proposed that the voids and grain boundaries within the SSEs, as well as the insufficient interfacial contact between Li and SSEs are the two main reasons for lithium dendrite formation in sulfide-based ASSLBs.[16,22] Thus, there should be a critical current density at which short-circuiting of the cell occurs in the Li_2S-P_2S_5 solid electrolyte system.[14,15] However, recent reports indicate that the Li dendrites can be formed in $Li_4Ti_5O_{12}$/Li_2S-P_2S_5/Li[20] and Se/Li_3PS_4/Li[21] ASSLBs using bare Li as the anode, even at a low current density of 50 mA g^{-1}. Another possible reason proposed by Wang and co-workers is the relatively high electronic conductivity (10^{-9}–10^{-8} S cm^{-1}) of Li_3PS_4.[16] Though not fully understood yet, the introduction of additives into SSEs similar to Li protection in liquid batteries have been developed. For example, LiI,[16] LiF,[23] and P_2O_5[24] have been introduced into Li_3PS_4 and proven to be effective suppressing lithium

Dr. J. Liang, Dr. X. Li, Dr. Y. Zhao, Dr. W. Li, K. R. Adair, Dr. M. N. Banis, Prof. T.-K. Sham, Dr. R. Li, Prof. X. Sun
Department of Mechanical and Materials Engineering
University of Western Ontario
1151 Richmond St, London, Ontario N6A 3K7, Canada
E-mail: xsun9@uwo.ca

Prof. L. V. Goncharova
Department of Physics and Astronomy
University of Western Ontario
1151 Richmond St, London, Ontario N6A 3K7, Canada

Dr. W. Li, Prof. T.-K. Sham
Department of Chemistry
University of Western Ontario
1151 Richmond St, London, Ontario N6A 3K7, Canada

Dr. M. N. Banis, Dr. Y. Hu
Canadian Light Source
44 Innovation Boulevard, Saskatoon, SK S7N 2V3, Canada

Dr. H. Huang
Glabat Solid-State Battery Inc.
700 Collip Circle, London, Ontario N6G 4X8, Canada

Dr. L. Zhang, Dr. S. Zhao, Dr. S. Lu
China Automotive Battery Research Institute Co. Ltd
5th Floor, No. 43, Mining Building, North Sanhuan Middle Road
Beijing 100088, China

The ORCID identification number(s) for the author(s) of this article can be found under https://doi.org/10.1002/aenm.201902125.

DOI: 10.1002/aenm.201902125

penetration across the Li_3PS_4 SSE layer. Without a method of protecting the SSEs interface, the evolution of an interfacial layer between sulfide SSEs and Li metal is caused by the reduction of sulfide-SSEs. Thus, the interfacial chemistry of the ASSLBs is a dominant factor in determining electrochemical performance and gives rise to the opportunity to develop new strategies to avoid lithium penetration.

Another challenge facing the application of Li metal is its demanding processing requirements. First, Li metal is readily corroded upon exposure to air due to the chemical reaction between Li and H_2O, N_2, O_2, CO_2. Therefore, it is difficult to use or store metallic Li for a long time even in a dry-air atmosphere. Moreover, the parasitic reaction of Li with air leads to a nonuniform and ion-impeding surface layer that causes deterioration of electrochemical performance and aggravates Li dendrite growth during cycling due to inhomogeneous electron/ionic current densities at the interface.[25] Until now, a few successful examples of air-stable Li anodes based on the surface coating have been reported.[25–32] For example, Li_2CO_3 coated Li microparticles are highly stable in dry room.[25–27] Al_2O_3 protected Li via atomic layer deposition was also reported to improve the stability under ambient conditions (40% relative humidity) for several hours.[28] Other artificial layers such as Li_2O has been proposed as passivating coatings to improve the air-stability of Li alloys.[29,30] A specific structure with densely packed Li alloy nanoparticles encapsulated by large graphene sheets has also been shown to possess enhanced air stability.[32] However, many coating layers such as Li_2CO_3, Al_2O_3, and Li_2O exhibit a very low ionic conductivity, which is detrimental to their use in ASSLBs as a result of the high interfacial resistance. In contrast to liquid-based batteries, the Li^+ conductivity of the protection layer in ASSLBs is essential since the fast electrochemical kinetics only can be guaranteed by effective Li^+ migration across the interfacial layer.[33–35] An air-stable and high ionic conductivity material as an artificial protection layer for Li anode in ASSLBs is therefore highly desired. Until now, the use of an air-stable Li anode is yet to be shown in ASSLBs.

Herein, we demonstrate the development of an air-stable Li anode with an in situ formed Li_xSiS_y layer on the surface based on solution reaction.[35,36] The Li_xSiS_y layer is fabricated by a simple two-step solution-based reaction process through the chemical reaction among Li, Li_2S_8, and silicon tetrachloride ($SiCl_4$) (**Figure 1**a). The in-depth compositions of the Li_xSiS_y layer were analyzed detailedly by combining synchrotron-based high energy X-ray photoelectron spectroscopy (HEXPS), time-of-flight secondary ion mass spectrometry (TOF-SIMS), and Rutherford backscattering spectrometry (RBS). The air-stable Li_xSiS_y protective layer can not only block the side reaction between Li and sulfide electrolyte but also allow excellent ion migration across the interface and stable cycling performance in sulfide-electrolyte-based ASSLBs. Symmetric cells configured with a Li_3PS_4 SSE and Li_xSiS_y protected Li (Li_xSiS_y-Li) electrodes show stable cycling up to 2000 h. Moreover, all-solid-state $LiCoO_2/Li_3PS_4/Li_xSiS_y$-Li cells show a capacity retention of 87.3% for 100 cycles compared to the limited 4 cycle lifetime of the cell using bare Li metal as the anode. These results not only prove the effectiveness of the Li_xSiS_y protection layer improving the stability of Li metal toward air and sulfide SSE, but also show a promising solution-based route for the in situ formation of protection layers with intimate contact and feasible fabrication process for ASSLBs.

2. Results and Discussion

2.1. Synthesis and Characterization

Figure 1a reveals the in situ fabrication process of the Li_xSiS_y layer on the surface of metallic Li by the reaction of Li, Li_2S_8, and $SiCl_4$ based on a two-step process (Figure 1a, R1, and R2). In order to obtain a uniform Li_xSiS_y layer, low concentration of Li_2S_8/tetrahydrofuran (THF) solution, $SiCl_4$/THF solution, low oxygen content, and a low moisture environment are necessary. Herein, all the reactions were performed in an Ar-filled glovebox (H_2O, O_2 <0.1 ppm). First, polished Li metal was dipped into a Li_2S_8/THF solution for 12 h to passivate the surface of Li and form a uniform polysulfide layer (Li_2S_x, R1). Subsequently, the $SiCl_4$/THF solution was added into the resulting solution and shook by hand for ≈10 min to perform the second step reaction (R2). The addition of Si–Cl functionality from $SiCl_4$ is designed to chemically react with Li_2S_x and Li metal to form a thermodynamic stable LiCl product and Li_xSiS_y. LiCl can be dissolved into THF solvent and removed after the cleaning process. Moreover, the thickness of the protected Li_xSiS_y layer can be adjusted by changing the concentration of Li_2S_8/THF and $SiCl_4$/THF solutions. Here, we choose to use one concentration (0.025 mol L^{-1}) of Li_2S_8/NMP solution as an example for detailed analysis (marked as Li-Li_xSiS_y-1, experimental details are shown in the Supporting Information). After the reaction and washing process, the surface of Li metal changes from metallic luster to gray. Scanning electron microscope (SEM) images of the bare Li electrode demonstrates a smooth and creaseless surface (Figure 1b). After the first reaction step, the surface of the Li electrode becomes more creased and some deposited material can be found (Figure S1, Supporting Information). Further treatment with the $SiCl_4$/THF solution and washing leads to the formation of the Li-Li_xSiS_y-1 electrode with a porous morphology (Figure 1c). X-ray diffraction (XRD) patterns of the Li-Li_xSiS_y-1 electrode still reveal the peaks of metallic Li which means that the protection layer is amorphous (Figure S2, Supporting Information).

X-ray photoelectron spectroscopy was further employed to confirm the composition of the Li_xSiS_y layer. Figure 1d–f shows the Li 1s, Si 2p, and S 2p XPS spectra of the Li-Li_xSiS_y-1 electrode. The XPS spectrum of the Li 1s can be fitted with a Gaussian component peak at 55.2 eV, which is related to Li—S bonds (Figure 1d). Moreover, the Si 2p spectrum exhibits several peaks, which can be fitted with two distinct doublets ($2p_{1/2}$ and $2p_{3/2}$) (Figure 1e). A special peak of the Si $2p_{3/2}$ appears at 101.4 eV (pink curves) which can be assigned to Li_2SiS_3 or Li_4SiS_4.[37] Correspondingly, the S 2p spectrum confirmed the proper assignment with the responsive peaks of S $2p_{3/2}$ at 161.5 eV (purple curves in Figure 1f). Due to the similar chemical valence of Si and S core in Li_2SiS_3 and Li_4SiS_4, the XPS peak of Li_2SiS_3 and Li_4SiS_4 component is too closed to be distinguished. Another peak in the Si 2p spectrum at 102.7 eV (dark cyan curves) should be related to the component of SiS_2.[37] The S 2p spectrum also suggests the presence of SiS_2 based

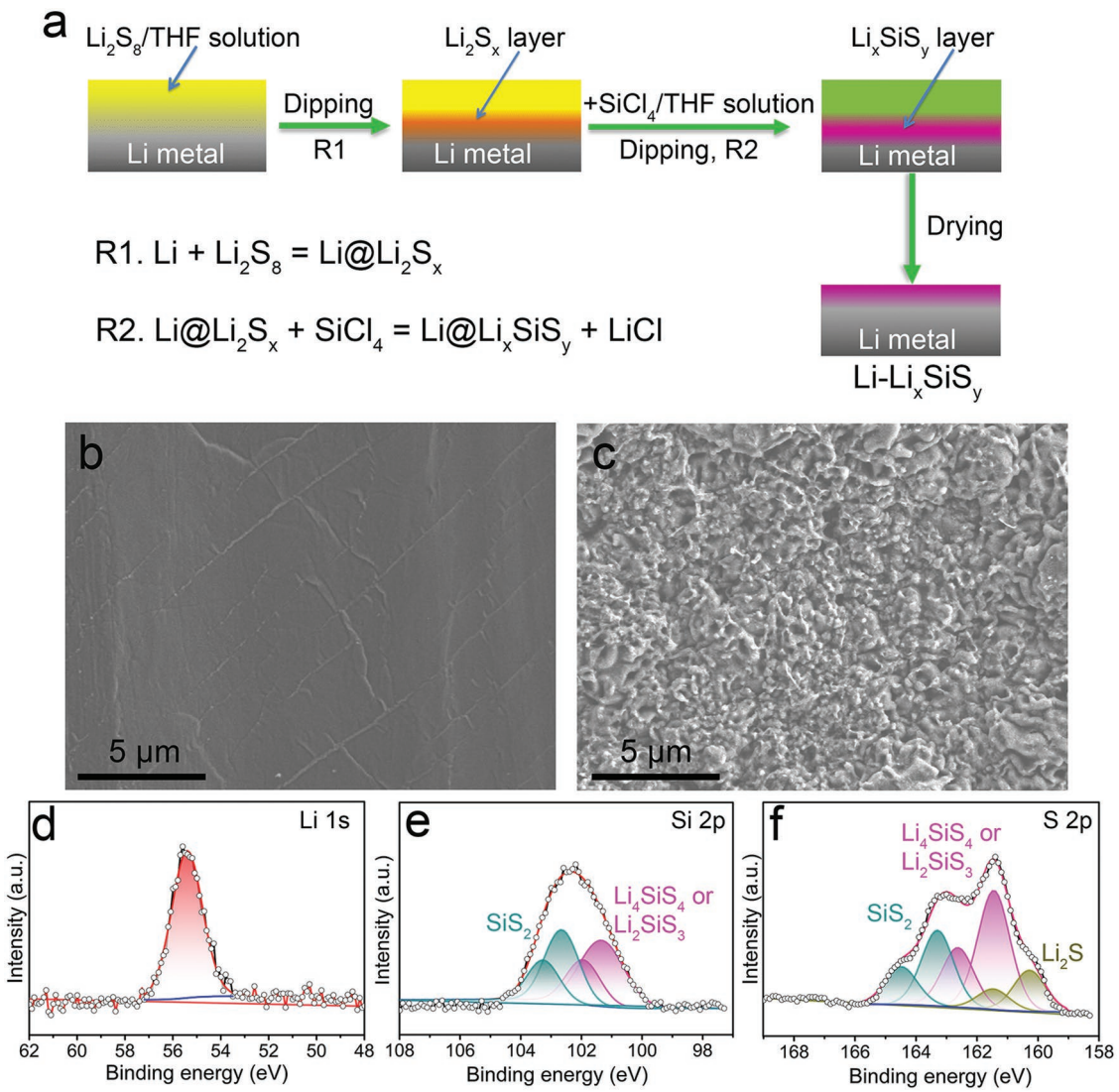

Figure 1. Reaction scheme for the formation of Li-Li_xSiS_y and the characterization of the Li-Li_xSiS_y-1 electrode. a) Schematic illustration of the in situ formation process of Li-Li_xSiS_y. SEM images of b) bare Li and c) Li-Li_xSiS_y-1 electrode. d–f) XPS analysis for the surface of Li-Li_xSiS_y-1.

on the S $2p_{3/2}$ at 163.3 eV (dark cyan curves in Figure 1f).[37] In addition, signals assigned to Li_2S in the spectra could also be observed (with S $2p_{3/2}$, 160.3 eV, yellow curves in Figure 1f). Thus, it can be concluded that the main chemical compositions of Li_xSiS_y protected layer are of Li_2SiS_3/Li_4SiS_4 and SiS_2 together with small amount of Li_2S.

Typically, conventional XPS using Al Kα (1486.6 eV) or Mg Kα (1256.8 eV) source has been used to study the chemical composition of the surface. However, the buried interfaces cannot be studied since the detection depth of the conventional XPS is limited to the first few nanometers in the near-surface region. The use of much higher energy (1.7–10 keV) from a synchrotron radiation source can significantly increase the electron escape depth for both photoelectrons and Auger electrons caused by their increased kinetic energy (**Figure 2**a). As a result, the tunable kinetic energies allow for variable depth analysis even up to several tens of nanometers. Thus, nondestructive high energy X-ray photoelectron spectroscopy of Li-Li_xSiS_y-1 foil was further conducted by using the soft X-ray microcharacterization beamline (SXRMB) at the Canadian Light Source. Figure 2b exhibits the Si 1s and S 1s spectra of the Li-Li_xSiS_y-1 foil excited by different photon energies ranging from 3 to 8 keV, which is related to the chemical composition from the surface to the coating at depth.

It can be observed that the Si 1s spectra obtained at 3–8 keV of the Li-Li_xSiS_y-1 foil are similar. Two typical peaks at 1842.6 and 1843.7 eV were observed, which can be assigned to SiS_2 and Li_4SiS_4 or Li_2SiS_3, respectively. For the S 1s spectra obtained at 3 keV, an obvious peak at ≈2477 eV caused by the oxidation species of sulfur at the surface of the Li-Li_xSiS_y-1 foil is present, which should be due to partial oxidation during transfer. The other three peaks at ≈2473, 2471, and 2469 eV are corresponding to SiS_2, Li_4SiS_4/Li_2SiS_3, and Li_2S, respectively. When the energy of the X-rays is increased, the signal due to oxidized species almost disappears. In contrast, the relative intensity ratio of Li_2S increases progressively at higher

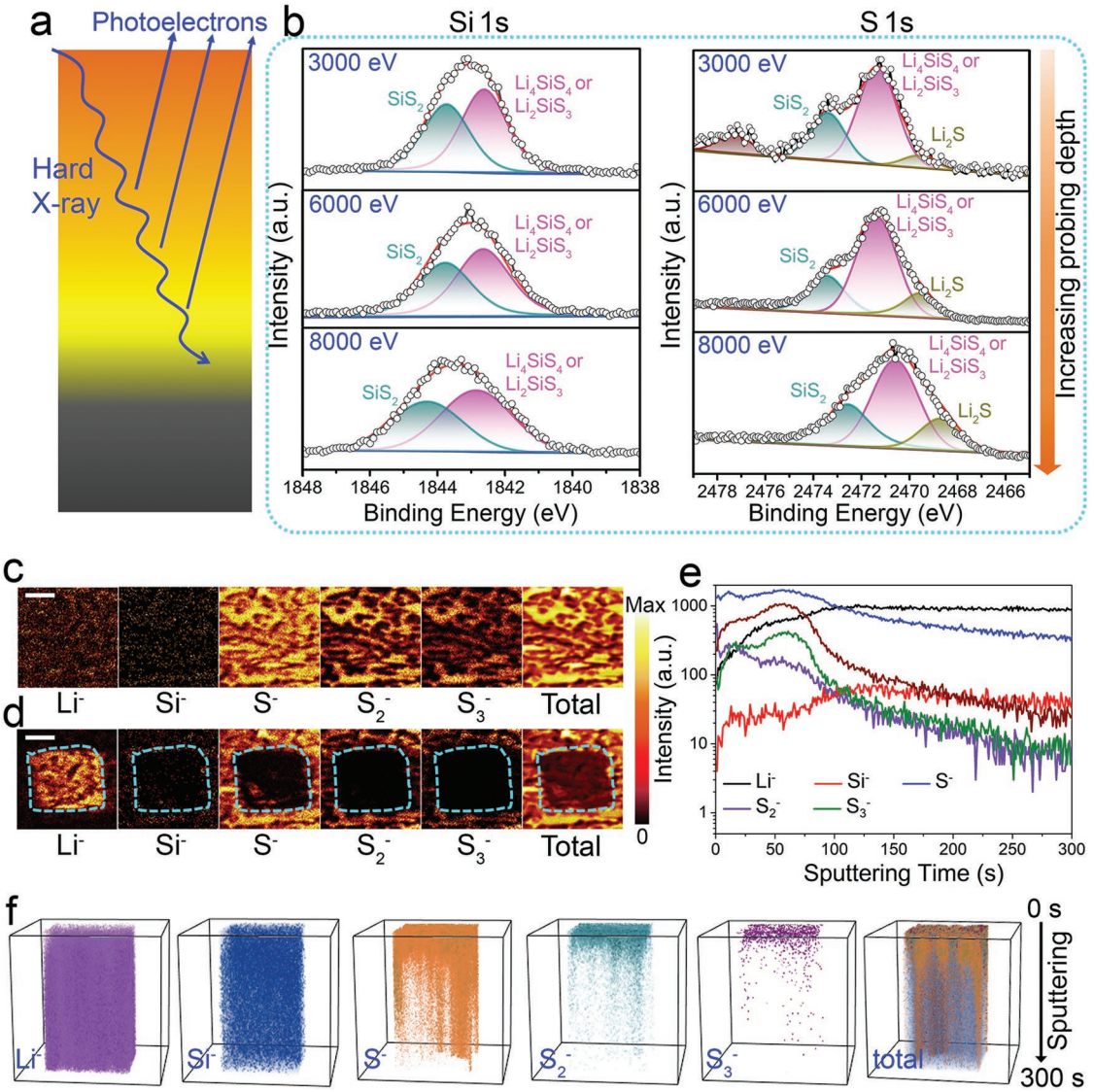

Figure 2. Depth characterizations of the Li-Li_xSiS_y electrodes. a) Schematic view of the evolution of the analysis depth as a function of the photon energy. b) HEXPS curves of the Li-Li_xSiS_y-1 electrodes at different energies from 3000 to 8000 eV. c,d) TOF-SIMS secondary ion images of Li-Li_xSiS_y-1 electrodes c) before and d) after Cs^+ consecutive sputtering for 300 s (the length of scale bar is 100 µm). e) Depth profile of various secondary ion species obtained by sputtering. f) The 3D view images of the sputtered volume corresponding to the depth profiles in (e).

photon energy hence longer probing depth. In addition, the peaks of SiS_2, Li_4SiS_4/Li_2SiS_3, and Li_2S slightly shift to lower energy with the increase in photon energy. The corresponding detailed position and intensities of these peaks are compared in Table S1 and S2 in the Supporting Information. The increase of Li_2S content at a greater depth might be caused by residual Li_2S_x species that is not fully reacted with the $SiCl_4$/THF solution in R2.

Time-of-flight secondary ion mass spectrometry was further performed to identify the compositions of the Li-Li_xSiS_y-1 foil and elemental depth distributions (Figure 2c–f). The TOF-SIMS spectra were collected over time from the ejected secondary ions sputtered by Cs^+; and the relative intensity is also related to the weight of the ejected ions. In the initial sputtering region (Figure 2c), a relatively uniform distribution of secondary ions from Li^-, Si^-, S^-, S_2^-, and S_3^- species was observed, demonstrating the successful formation of a Li_xSiS_y coating on the surface of Li metal. After sputtering for 300 s, the intensity of Li^- is significantly increased, while the opposite trend was presented for the most of other species (Figure 2d). The intensity variation is clarified in Figure 2e,f. Clearly, the signals of S^-, S_2^-, and S_3^- are relatively high on the surface layer and reduce in the inner layers. While, the signal of Si^- increases along with the sputtering time up to 100 s and then remains steady up to 300 s. The results indicate that the thickness of Li_xSiS_y layer should be more than 30 nm estimated by the sputtering rate of 0.1 nm s^{-1}. Moreover, Rutherford backscattering spectrometry of Li-Li_xSiS_y-1 foil was performed to evaluate its thickness. The obvious presence of Si and S peaks in the RBS spectra and simulation profiles in Figure S3 in

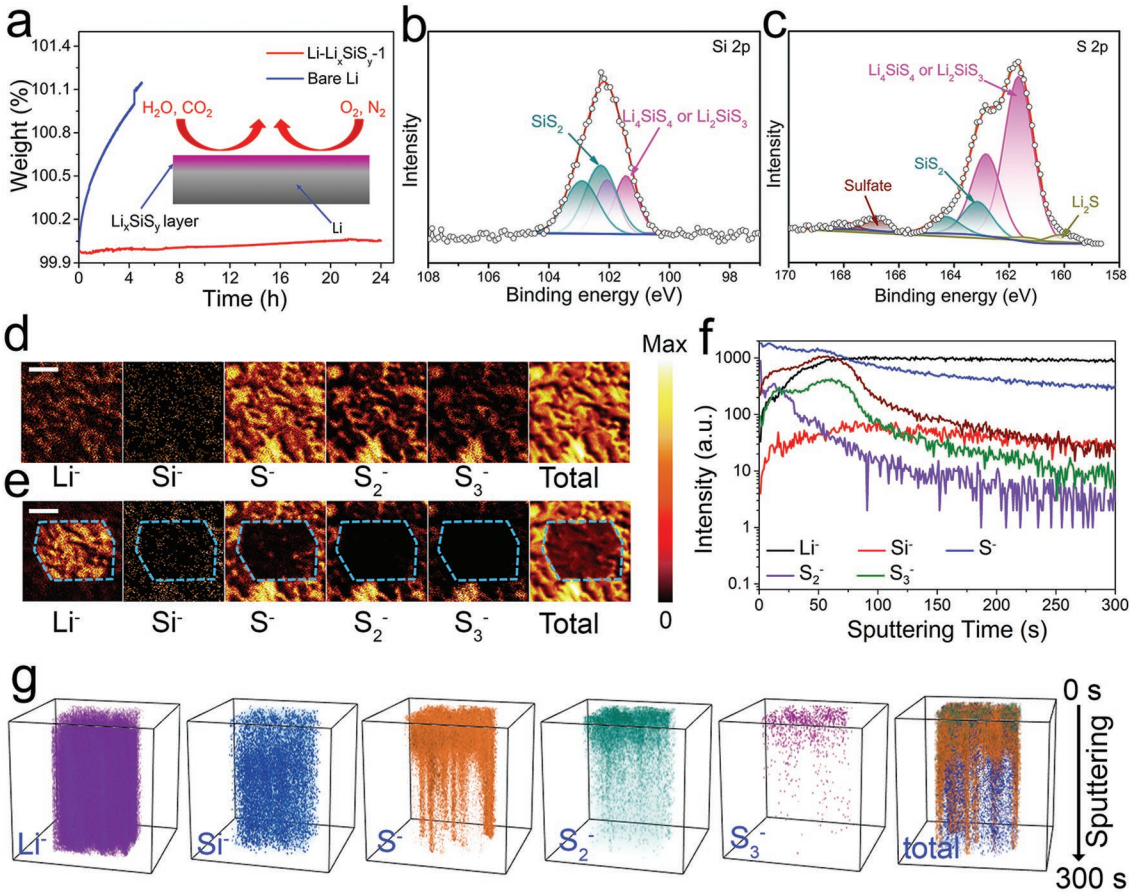

Figure 3. Air stability of Li-Li$_x$SiS$_y$-1 electrode. a) Thermal gravimetric analysis of the Li-Li$_x$SiS$_y$-1 electrode and bare Li electrode in air over time, inset is the schematic representation of the Li$_x$SiS$_y$ layer as a protection layer for blocking the chemical reaction between Li and air. b,c) XPS spectra of Li-Li$_x$SiS$_y$-1 electrodes after ambient air exposure for 5 h. b) Si 2p spectra; c) S 2p spectra. d,e) TOF-SIMS secondary ion images of air-exposed Li-Li$_x$SiS$_y$-1 electrodes d) before and e) after Cs$^+$ consecutive sputtering for 300 s (the length of scale bar is 100 µm). f) Depth profile of various secondary ion species obtained by sputtering. g) The 3D view images of the sputtered volume corresponding to the depth profiles in (f).

the Supporting Information confirm the successful formation of Li$_x$SiS$_y$ protection layer on the Li. The O signal should be due to the air exposure during transfer process. The calculated depth profiles based on RBS spectra indicated that the thickness of Li$_x$SiS$_y$ layer on the surface Li-Li$_x$SiS$_y$-1 foil is ≈150 nm. Combined with the HEXPS, TOF-SIMS, and RBS analyses, it can be confirmed that the Li$_x$SiS$_y$ layer consists of Li$_2$SiS$_3$/Li$_4$SiS$_4$, SiS$_2$, and small amount of Li$_2$S. The ratio of those components varied with the depth of the Li$_x$SiS$_y$ layer, and the Li$_2$S increased as sputtering time progressed. Based on the theory proposed by Wang and co-workers,[9] the electronic conductivity of these components is quite low, and the Li$_2$SiS$_3$/Li$_4$SiS$_4$ components guarantee fast Li$^+$ migration across the interfacial layer, indicating that the Li$_x$SiS$_y$ layer should be a promising Li protection layer in ASSLBs.

2.2. Air Stable Performance

Theoretically, these components in the Li$_x$SiS$_y$ layer are chemically inert and impermeable to dry-air and robust against oxidation,[38,39] suggesting that the use of Li$_x$SiS$_y$ layer as a protection layer for Li electrode could effectively block the parasitic side reaction in an ambient environment (**Figure 3**a). Thermal gravimetric analysis (TGA) was first employed to reveal the extent of the chemical reactions between Li and dry-air. The corresponding TGA curves of the bare Li and Li-Li$_x$SiS$_y$ foil under the dry-air atmosphere for hours at 25 °C are shown in Figure 3a. An ≈1.1% weight increase could be found after 6 h for bare Li foils under the dry-air flow (100 mL min^{-1}). Meanwhile, there is almost no weight change observed for the Li-Li$_x$SiS$_y$ foil during 24 h under the same condition. It can be concluded that Li-Li$_x$SiS$_y$ foil is more stable than bare Li foil in a dry-air atmosphere.

The chemical composition of the Li-Li$_x$SiS$_y$-1 foil after ambient air (humidity around 30%) exposure was further carried out by XPS (Figure 3b,c). The Si 2p spectra (Figure 3b) displayed two doublets (2p$_{1/2}$ and 2p$_{3/2}$). The peaks of Si 2p$_{3/2}$ at 101.4 eV are corresponding to the existence of Li$_4$SiS$_4$/Li$_2$SiS$_3$, and the S 2p spectrum (Figure 3c) further validates the assignment with a peak at 161.4 eV that should be assigned to Li$_4$SiS$_4$/Li$_2$SiS$_3$. There is another peak in the Si 2p spectrum located at 102.3 eV (dark cyan curves, Si 2p$_{3/2}$), which is related to the formation of SiS$_2$. Correspondingly, the S 2p spectrum also

suggests the presence of SiS_2 based on the S $2p_{3/2}$ at 163.3 eV (dark cyan curves in Figure 3c).[37] In addition, the S 2p spectrum still contains several weak doublet (S $2p_{1/2}$ and $2p_{3/2}$) peaks which are related to the presence of Li_2S and sulfate. It can be concluded that these peaks are similar to the pristine Li-Li_xSiS_y-1 electrode without air exposure. The observation of relatively lower intensity of SiS_2 and Li_2S species should be caused by their instability toward humidity. Moreover, the TOF-SIMS mapping images of Li-Li_xSiS_y-1 after ambient air exposure (Figure 3d,e) and elemental depth distributions (Figure 3f,g) collected from the ejected secondary ions sputtered by Cs^+ were also similar to the results of the freshly prepared Li-Li_xSiS_y-1 foil shown in Figure 2c–f, further demonstrating the stability of Li_xSiS_y layer in air.

2.3. Li Plating and Stripping Performance

To study the electrochemical properties of the Li-$LiSi_xS_y$ electrodes, symmetric all-solid-state Li cells were fabricated with commercial Li_3PS_4 as the solid-state electrolyte. Two other Li-Li_xSiS_y foils with Li_xSiS_y protection layers of different thicknesses were also tested (detailed synthesis is shown in the Supporting Information). The thickness of the Li_xSiS_y layer was controlled by utilizing different concentrations of Li_2S_8/THF and $SiCl_4$/THF solutions. Correspondingly, the Li-Li_xSiS_y foils were denoted as Li-Li_xSiS_y-0.25 and Li-Li_xSiS_y-0.5 based on the concentration of the reaction solution. SEM and XRD patterns of these samples are demonstrated in Figure S4–S6 in the Supporting Information. It is revealed that all of these samples show a similar porous and amorphous structure with the same XRD peaks. RBS results in Figure S7 in the Supporting Information proved the thicker Li_xSiS_y layer on the surface for Li-Li_xSiS_y-1 compared to that of Li-Li_xSiS_y-0.25.

Figure 4 shows the charge/discharge profiles at a constant current of 0.1 mA cm^{-2} and a capacity of 0.5 mAh cm^{-2} for bare Li and Li-$LiSi_xS_y$ electrodes. For the symmetrical all-solid-state Li cells, commercial Li_3PS_4 as SSEs suffer from a short cycling life due to the dendritic formation of Li as shown in Figure 4a, which is consistent with previous reports.[9,21] All of the

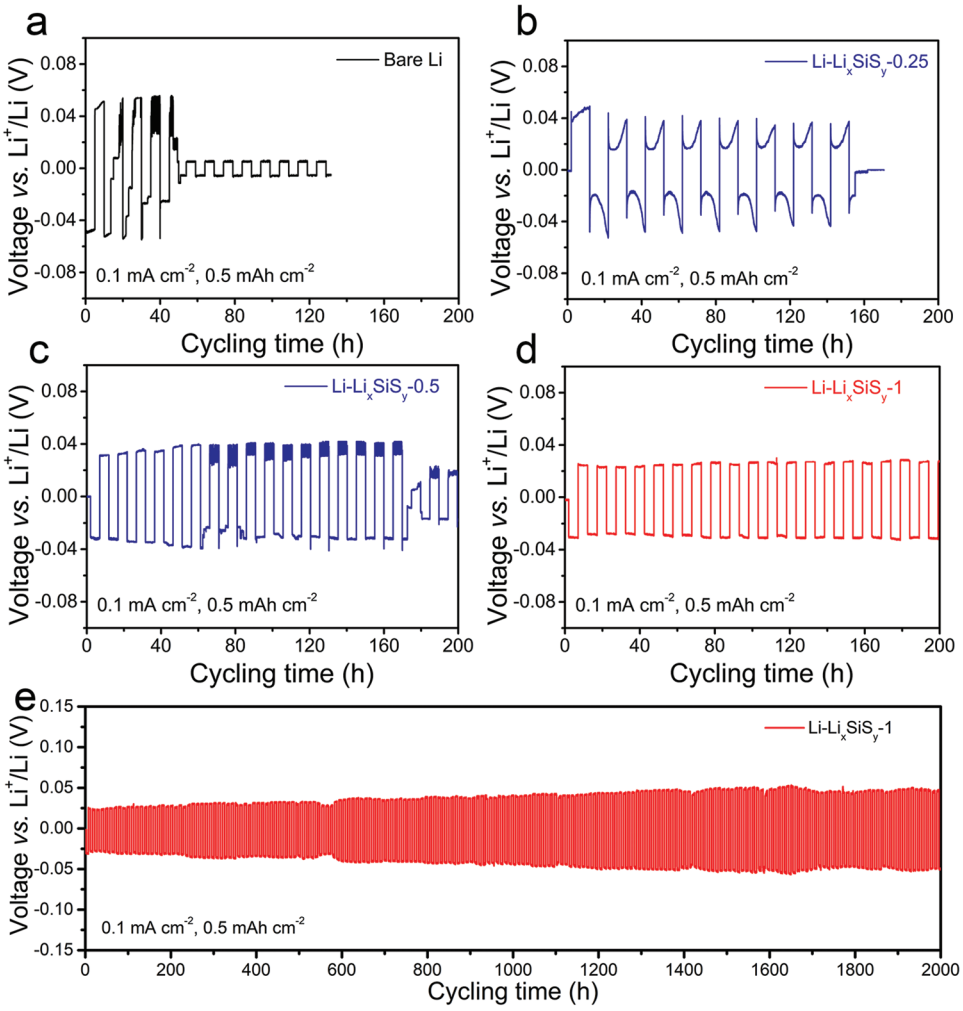

Figure 4. Electrochemical performance of the symmetric solid-state Li-Li_xSiS_y cells and symmetric bare Li cell by using Li_3PS_4 as the electrolyte. Galvanostatic charge/discharge curves of the a) symmetric bare Li cell, b) symmetric Li-Li_xSiS_y-0.25 cell, c) symmetric Li-Li_xSiS_y-0.5 cell, and d) symmetric Li-Li_xSiS_y-1 cells. e) Long-term cycling performance of symmetric Li-Li_xSiS_y-1 cells.

symmetrical all-solid-state Li cells based on Li-LiSi$_x$S$_y$ electrodes exhibited improved Li stripping/platting performance, while there is still a short-circuiting phenomenon for Li-Li$_x$SiS$_y$-0.25 and Li-Li$_x$SiS$_y$-0.5 electrodes (Figure 4b,c). The most stable performance could be achieved for Li-Li$_x$SiS$_y$-1 electrodes as presented in Figure 4d,e. The symmetric Li-Li$_x$SiS$_y$-1 cells exhibited an initial overpotential around ≈25 mV at 0.1 mA cm^{-2}. No short circuit phenomenon was observed even for 2000 h just with only a slight increase in overpotential. Furthermore, the cross section SEM images of Li/Li$_3$PS$_4$ and Li-Li$_x$SiS$_y$-1/Li$_3$PS$_4$ after 10 cycles are compared in Figure S8 in the Supporting Information. It can be seen that the close contact between Li-Li$_x$SiS$_y$-1 electrode and Li$_3$PS$_4$ electrolyte after cycling, while obvious cracks between bare Li electrode and Li$_3$PS$_4$ electrolyte was observed, which might be caused by the uneven lithium plating/stripping. The rate capability of the symmetrical cell at different current densities up to 1 mA cm^{-2} are presented in Figure S9 in the Supporting Information and also indicates relatively stable voltage polarization. The results demonstrate that the protection of Li-Li$_x$SiS$_y$ layer could effectively inhibit short-circuiting for Li$_3$PS$_4$ SSEs in all-solid-state cells, and the thickness of the protection layer also plays a key role in the performance of all-solid-state symmetric cells.

2.4. Composition Evolution upon Electrochemical Cycling

In order to reveal the underlying mechanism of the improved electrochemical performances, we further studied the composition evolution of the bare Li and Li-LiSi$_x$S$_y$ electrodes after cycling. To analyze the interlayer composition between Li or Li-Li$_x$SiS$_y$ electrode and Li$_3$PS$_4$ SSEs after cycling, symmetric cells with Li and Li-LiSi$_x$S$_y$-1 electrodes cycled at 0.5 mA cm^{-2} for 200 cycles were disassembled inside a glove-box for XPS analysis. The intensity of P 2p spectra for bare Li electrode is much higher than that of the Li-LiSi$_x$S$_y$-1 electrode (Figure S10, Supporting Information), indicating the more severe interfacial reactions between bare Li and Li$_3$PS$_4$ SSEs occur. As presented in **Figure 5**a, two sets of the phosphorous species assigned to −P−S−P− and Li−P−S species could

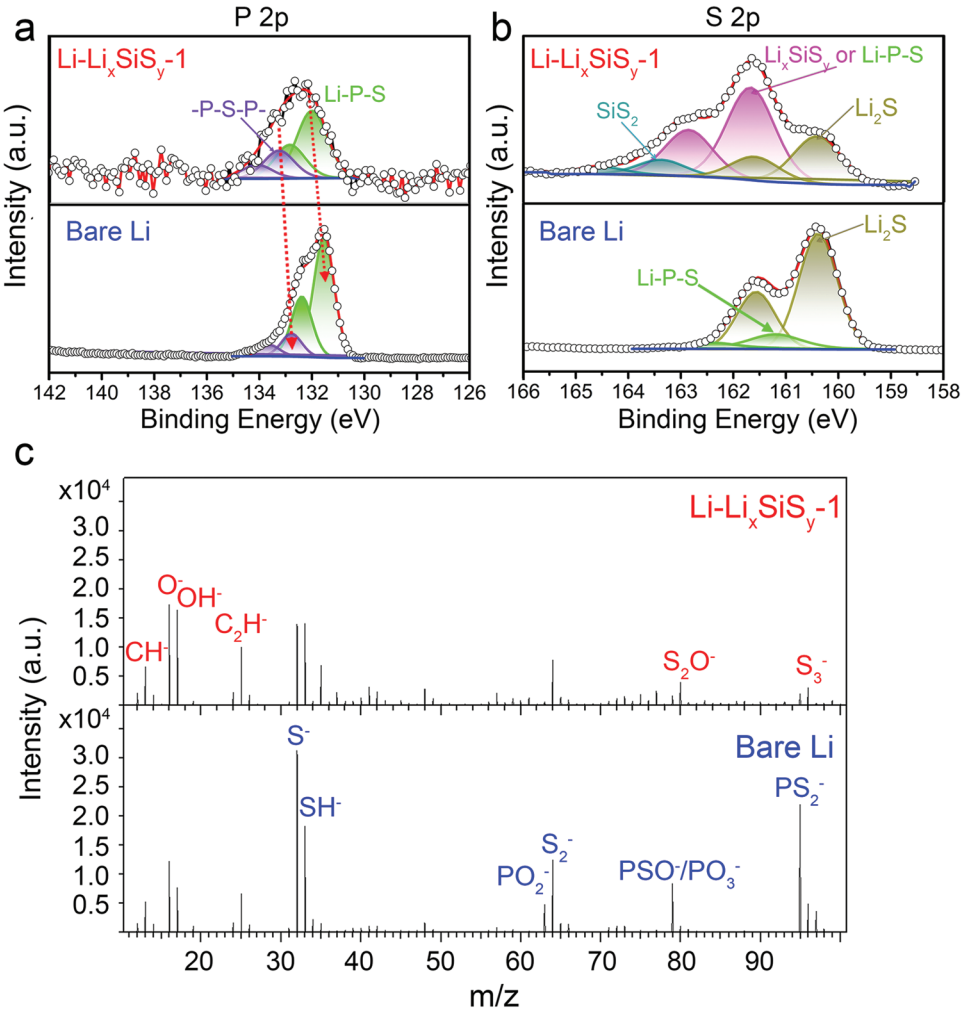

Figure 5. XPS characterization of bare Li and Li-Li$_x$SiS$_y$-1 electrodes after 200 h at 0.1 mA cm^{-2} for 0.5 mAh cm^{-2}. a) P 2p spectra; b) S 2p spectra. TOF-SIMS spectra of bare Li and Li-Li$_x$SiS$_y$-1 electrode after 200 h at 0.1 mA cm^{-2} for 0.5 mAh cm^{-2}.

be identified for both samples, which are marked purple and green located at 131.7–131.9 and 132.7–132.9 eV, respectively. Furthermore, the binding energy of the bare Li sample shifts to lower energy compared to that of Li-LiSi$_x$S$_y$-1 electrode, which should be caused by the reduction of Li_3PS_4 SSEs after direct contact with Li metal. Moreover, the Li-LiSi$_x$S$_y$-1 electrode still displays similar Si 2p and S 2p spectra as shown in Figure S11 in the Supporting Information and Figure 5b with the exception of changes in relative intensity. It should be noted that S 2p3/2 peak centered at ≈161.5 eV here should be assigned not only to Li_2SiS_3/Li_4SiS_4 but also to Li—P—S species from the Li_3PS_4 SEs. For the S 2p spectrum of bare Li metal, the dominant peaks are attributed to Li_2S, demonstrating that the Li_3PS_4 SSEs in direct contact with Li was reduced. The compositions were further studied by TOF-SIMS (Figure 5c). The surface of bare Li or Li-LiSi$_x$S$_y$-1 that is in direct contact with Li_3PS_4 SSEs was first sputtered by Cs^+ ions. The existence of CH^-, O^-, OH^-, and C_2H^- species for both samples should be due to the air exposure during transfer. Obviously, strong peaks due to PO_2^-, PSO^-/PO_3^-, and PS_2^- species could be observed for bare Li, indicating that there should reaction between bare Li and Li_3PS_4 SSEs during the plating/stripping tests. Comparatively, only a weak signal of S_2O^- and S_3^- for Li-LiSi$_x$S$_y$-1 electrode is observed after cycling, which should originate from the Li$_x$SiS$_y$ protection layer since there are no phosphorous species. Based on the surface XPS and sputtered samples with TOF-SIMS results, the Li$_x$SiS$_y$ protection layer with optimized thickness could prevent the side reaction between Li and Li_3PS_4 SSEs that might induce dendrite growth and short circuits.

2.5. All Solid-State Li Batteries Performance

The Li electrode with and without Li$_x$SiS$_y$ layer was used for more in-depth electrochemical studies in full ASSLBs in which the bare Li and Li-Li$_x$SiS$_y$ anodes were paired with a commercial $LiCoO_2$ (LCO) cathode and Li_3PS_4 as SSEs. The detailed assembly process of the full Li-LCO ASSLBs is shown in the Experimental Section. Indeed, the Li-Li$_x$SiS$_y$ anode shows significantly improved cycling performance than that of the cell with the pristine Li anode. As shown in **Figure 6**a, the full Li-LCO ASSLBs with pristine Li as the anode is only stable for the initial 50 h at 0.13 mA cm^{-2} (approximately three charge/discharge cycles). After three cycles, the cell exhibits a serious overcharge process which is marked by red arrows in Figure 6a. The overcharge process is related to short-circuiting of the Li anode during charging process. It is one of the reasons why pristine Li is not suitable for ASSLBs when using sulfide as the electrolyte and most of the research is focused on $Li_4Ti_5O_{12}$, indium, or other kinds of alloy as the anode, although Li have the highest energy density. Compared to the pristine Li anode, the Li-LCO ASSLBs with Li-Li$_x$SiS$_y$ anode reveal a much more stable cycling performance without any overcharging for over 100 cycles (Figure 6b–d). As shown in Figure 6c, it can be revealed that the charge and discharge curves of the full Li-LCO all-solid-state cell with Li-Li$_x$SiS$_y$ as anode is stable and the capacity is higher than that with pristine Li (Figure 6a). The initial discharge capacity of the Li-LCO ASSLBs with Li-Li$_x$SiS$_y$ anode reaches 126 mAh g^{-1} at 0.13 mA cm^{-2} and remains at 110 mAh g^{-1} after 100 cycles (Figure 6d). From these results, it can be concluded that the Li$_x$SiS$_y$ protection layer on the surface

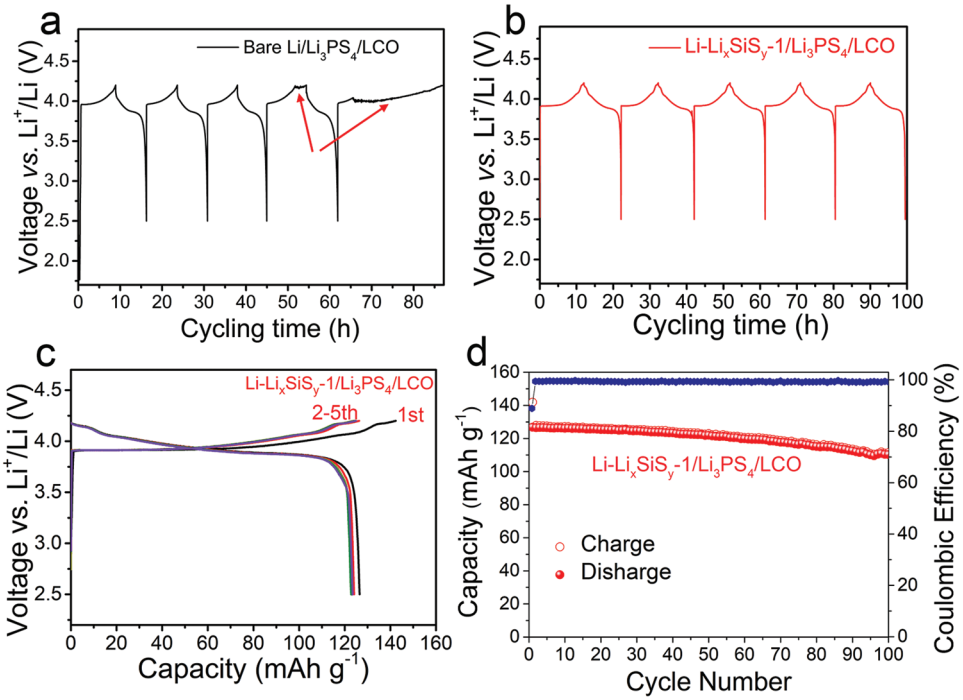

Figure 6. Electrochemical performance of an all-solid-state bare Li/Li_3PS_4/LCO cell and Li-Li$_x$SiS$_y$/Li_3PS_4/LCO cell. a) Charge and discharge curves of Li/Li_3PS_4/LCO cell, b) charge and discharge curves of Li-Li$_x$SiS$_y$/Li_3PS_4/LCO cell, c) charge and discharge curves of Li-Li$_x$SiS$_y$/Li_3PS_4/LCO cell at different cycles, and d) cycling performance of Li-Li$_x$SiS$_y$/Li_3PS_4/LCO at a current density of 0.13 mA cm^{-2}.

of Li metal can effectively avoid dendrite formation and short circuits both in all-solid-state symmetric cells and full cells with high-voltage cathodes. Moreover, even the all-solid-state symmetric cells and full cells with Li-Li_xSiS_y-1 anode after air exposure can show good electrochemical performance as shown in Figure S12 in the Supporting Information, indicating that the Li_xSiS_y protection layer can also improve the air-stability of Li metal.

3. Conclusions

In summary, we have successfully demonstrated that the in situ formed Li_xSiS_y protection layer on the surface of Li can stabilize the Li_3PS_4/Li interface. Moreover, the Li_xSiS_y protection layer is stable toward air. In-depth analyses using synchrotron HEXPS, TOF-SIMS, and RBS confirm the compositions of different chemical species within the Li_xSiS_y protection layer. The Li_2SiS_3/Li_4SiS_4 species ensure fast ionic migration across the protection layer, and the Li_2S in contact with Li metal prevent further interfacial reactions. Thus, the Li_xSiS_y protection layer can effectively prevent the reduction of Li_3PS_4 by Li metal. The symmetric cells with Li_xSiS_y protected Li anodes show steady cycling for over 2000 h. Moreover, $LiCoO_2/Li_3PS_4/Li_xSiS_y$-Li ASSLBs display good cycling performance over 100 cycles. This display of the in situ formation of a protective layer can solve the intrinsic challenges associated with sulfide SSEs in ASSLBs, and opens opportunities for the development of next-generation high-energy ASSLBs.

4. Experimental Section

Materials: Sulfur (S, sublimate), lithium sulfide (Li_2S, 99%), tetrahydrofuran, and silicon tetrachloride were purchased from Aladdin Industrial Corporation (USA); lithium foil (diameter was 10 mm and thickness was 250 µm) was purchased from China Energy Lithium Co., Ltd. Commercial $LiCoO_2$ electrode materials came from China Automotive Battery Research Institute (China). Commercial Li_3PS_4 electrolyte was purchased from MSE supplies LLC.

Preparation of Li-Li_xSiS_y Electrode: The Li_xSiS_y protection layer on the surface of Li metal was synthesized by using the two steps in situ reaction between Li_2S_8, $SiCl_4$, and Li in THF solvent based on the following two reaction equations

$$Li + Li_2S_8 = Li@Li_2S_x \quad (1)$$

$$Li@Li_2S_x + SiCl_4 = Li@Li_xSiS_y \quad (2)$$

In order to obtain a uniform Li_xSiS_y layer on the surface of Li metal, low concentrations of Li_2S_8/THF and $SiCl_4$/THF solutions, low oxygen content, and a low moisture environment are necessary. Here, all the reactions were performed in Ar-filled glove-box (H_2O, O_2 < 0.1 ppm). Typically, 23 mg Li_2S, 112 mg S, and 20 mL THF solvent was added into a glass bottle and stirred for 12 h to make a clear Li_2S_8/THF solution (0.025 mol L^{-1}). 0.12 mL $SiCl_4$ was added into 20 mL THF solution to form a clear $SiCl_4$/THF solution (≈0.05 mol L^{-1}). The first reaction step was using Li_2S_8 and metallic Li. A piece of metallic Li foil (polished by a toothbrush) and 1 mL of Li_2S_8/THF solution were added together into a clean glass bottle, following by standing for 12 h. The color of the solution was yellow and did not change during the standing process. This reaction was very slow, and followed by the addition of 1 mL $SiCl_4$/THF solution into the resulting solution. The solution was shaken by hand for ≈10 min to perform the second step reaction. When adding $SiCl_4$/THF solution, the color of the solution changed from yellow to pale yellow. After shaking, the color of the solution changed to bright yellow, which indicated the completion of the reaction. Then, the resulting Li foil was further washed with THF solvent and then dried for 1 h at 60 °C in Ar-filled glove-box. The surface color of the resulting Li foil changed from a shiny metal luster to gray. In order to control the thickness of the Li_xSiS_y layer, the concentration of the Li_2S_8/THF solution was changed from 0.25, 0.5, and 1 time of 0.025 mol L^{-1}. (The concentration of the $SiCl_4$/THF solution was two times of the concentration of Li_2S_8/THF solution.) The achieved Li-Li_xSiS_y foil was marked as Li-Li_xSiS_y-0.25, Li-Li_xSiS_y-0.5, and Li-Li_xSiS_y-1 based on the concentration of Li_2S_8/THF solution.

Characterizations: The structure and morphology of the as-prepared Li-Li_xSiS_y were characterized by X-ray diffractometer (Philips X'Pert Super diffractometer with Cu Ka radiation) and scanning electron microscopy (a Hitachi S-4800). The chemical information of the as-prepared Li-Li_xSiS_y foil was characterized by X-ray photoelectron spectrometer (ESCALAB 250 spectrometer, Perkin-Elmer). The XPS spectra were fitted with Gaussian–Lorentzian functions and a Shirley-type background. The spin–orbit split peaks for Si 2p ($2p_{1/2}$, $2p_{3/2}$) were constrained using a separation of 0.86 eV and the intensity ratio of $2p_{1/2}$:$2p_{3/2}$ about 0.52. The spin–orbit split peaks for S 2p ($2p_{1/2}$, $2p_{3/2}$) were constrained using a separation of 1.21 eV and the intensity ratio of $2p_{1/2}$:$2p_{3/2}$ about 0.54. The chemical information of the as-prepared Li-Li_xSiS_y foil with deep profile was tested by time-of-flight secondary ion mass spectrometry, Rutherford backscattering spectrometry, and high-energy X-ray photoelectron spectroscopy. The TOF-SIMS measurements were performed on an ION-TOF (GmbH, Germany) ToF-SIMS IV with a bismuth liquid metal ion source, the pressure of the chamber was around 10^{-8} mbar. Sputtering with a Cs^+ ion beam (3 keV) was applied for depth profiling analysis, corresponding to sputtering areas of 100 × 100 µm^2. The thickness of Li_xSiS_y layer was characterized by RBS using 1 and 2 MeV He^+ beam (Western Tandetron Facility at University of Western Ontario) at several locations on the surface. A Sb-implanted amorphous Si sample (with Sb content of 4.82×10^{15} atoms cm^{-2}) was used for calibration. High-energy X-ray photoelectron spectroscopy was performed on the soft X-ray microcharacterization beamline at the CLS30 under different energies.

Electrochemical Characterizations: Symmetrical all-solid-state Li/Li_3PS_4/Li cells were assembled with bare Li metal and Li_xSiS_y protected Li as the electrodes, and commercial Li_3PS_4 as the solid-state electrolyte layer. The cathode composites were prepared by hand mixing process of $LiNbO_x$ coated $LiCoO_2$[40] and Li_3PS_4 in a weight ratio of 7:3. For the assembly of ASSLBs with $LiCoO_2$ cathodes, the solid-state electrolyte layer was prepared by pressing 100 mg of Li_3PS_4 at 2 ton inside a polytetrafluoroethylene (PTFE) die (diameter of 10 mm). Then, 10 mg of the cathode composites were dispersed on the surface of the solid-state electrolyte uniformly and pressed at 2 ton. Finally, one piece of bare Li anode or Li_xSiS_y protected Li was attached on the other side of the solid-state electrolyte layer and pressed at 1 ton. The active $LiCoO_2$ loading was about 8.92 mg cm^{-2}. All the electrochemical tests were conducted using a Land cycler (Wuhan, China) at room temperature.

Supporting Information

Supporting Information is available from the Wiley Online Library or from the author.

Acknowledgements

J.L. and X.L. contributed equally to this work. This work was supported by the Natural Science and Engineering Research Council of Canada (NSERC), the Canada Research Chair Program (CRC), the Ontario Research Fund, the Canada Foundation for Innovation (CFI), the China

Automotive Battery Research Institute Co., Canada MITACS fellowships, the Canada Light Source at University of Saskatchewan (CLS), and the University of Western Ontario.

Conflict of Interest

The authors declare no conflict of interest.

Keywords

air stable, all-solid-state batteries, Li_3PS_4, lithium metal anodes, sulfide electrolytes

Received: July 1, 2019
Revised: July 28, 2019
Published online:

[1] Y. Guo, H. Li, T. Zhai, *Adv. Mater.* **2017**, *29*, 1700007.
[2] J. C. Bachman, S. Muy, A. Grimaud, H.-H. Chang, N. Pour, S. F. Lux, O. Paschos, F. Maglia, S. Lupart, P. Lamp, L. Giordano, Y. Shao-Horn, *Chem. Rev.* **2016**, *116*, 140.
[3] C. Yang, K. Fu, Y. Zhang, E. Hitz, L. Hu, *Adv. Mater.* **2017**, *29*, 1701169.
[4] J. Janek, W. G. Zeier, *Nat. Energy* **2016**, *1*, 16141.
[5] N. Kamaya, K. Homma, Y. Yamakawa, M. Hirayama, R. Kanno, M. Yonemura, T. Kamiyama, Y. Kato, S. Hama, K. Kawamoto, *Nat. Mater.* **2011**, *10*, 682.
[6] Y. Kato, S. Hori, T. Saito, K. Suzuki, M. Hirayama, A. Mitsui, M. Yonemura, H. Iba, R. Kanno, *Nat. Energy* **2016**, *1*, 16030.
[7] M. A. Kraft, S. Ohno, T. Zinkevich, R. Koerver, S. P. Culver, T. Fuchs, A. Senyshyn, S. Indris, B. J. Morgan, W. G. Zeier, *J. Am. Chem. Soc.* **2018**, *140*, 16330.
[8] P. Adeli, J. D. Bazak, K. H. Park, I. Kochetkov, A. Huq, G. R. Goward, L. F. Nazar, *Angew. Chem., Int. Ed.* **2019**, *58*, 8681.
[9] F. Han, A. S. Westover, J. Yue, X. Fan, F. Wang, M. Chi, D. N. Leonard, N. J. Dudney, H. Wang, C. Wang, *Nat. Energy* **2019**, *4*, 187.
[10] C. Wang, Y. Zhao, Q. Sun, X. Li, Y. Liu, J. Liang, X. Li, X. Lin, R. Li, K. R. Adair, L. Zhang, R. Yang, S. Lu, X. Sun, *Nano Energy* **2018**, *53*, 168.
[11] Y. Gao, D. Wang, Y. C. Li, Z. Yu, T. E. Mallouk, D. Wang, *Angew. Chem., Int. Ed.* **2018**, *57*, 13608.
[12] Z. Zhang, S. Chen, J. Yang, J. Wang, L. Yao, X. Yao, P. Cui, X. Xu, *ACS Appl. Mater. Interfaces* **2018**, *10*, 2556.
[13] M. Nagao, A. Hayashi, M. Tatsumisago, T. Kanetsuku, T. Tsuda, S. Kuwabata, *Phys. Chem. Chem. Phys.* **2013**, *15*, 18600.
[14] R. Garcia-Mendez, F. Mizuno, R. Zhang, T. S. Arthur, J. Sakamoto, *Electrochim. Acta* **2017**, *237*, 144.
[15] L. Porz, T. Swamy, B. W. Sheldon, D. Rettenwander, T. Frömling, H. L. Thaman, S. Berendts, R. Uecker, W. C. Carter, Y. M. Chiang, *Adv. Energy Mater.* **2017**, *7*, 1701003.
[16] F. Han, J. Yue, X. Zhu, C. Wang, *Adv. Energy Mater.* **2018**, *8*, 1703644.
[17] H.-D. Lim, H.-K. Lim, X. Xing, B.-S. Lee, H. Liu, C. Coaty, H. Kim, P. Liu, *Adv. Mater. Interfaces* **2018**, *5*, 1701328.
[18] H. J. Deiseroth, S. T. Kong, H. Eckert, J. Vannahme, C. Reiner, T. Zaiss, M. Schlosser, *Angew. Chem., Int. Ed.* **2008**, *47*, 755.
[19] C. Yu, L. van Eijck, S. Ganapathy, M. Wagemaker, *Electrochim. Acta* **2016**, *215*, 93.
[20] M. Nagao, A. Hayashi, M. Tatsumisago, *Electrochem. Commun.* **2012**, *22*, 177.
[21] X. Li, J. Liang, X. Li, C. Wang, J. Luo, R. Li, X. Sun, *Energy Environ. Sci.* **2018**, *11*, 2828.
[22] Y. Shen, Y. Zhang, S. Han, J. Wang, Z. Peng, L. Chen, *Joule* **2018**, *2*, 1674.
[23] X. Fan, X. Ji, F. Han, J. Yue, J. Chen, L. Chen, T. Deng, J. Jiang, C. Wang, *Science Adv.* **2018**, *4*, 9245.
[24] Y. Tao, S. Chen, D. Liu, G. Peng, X. Yao, X. Xu, *J. Electrochem. Soc.* **2016**, *163*, A96.
[25] T. Yang, P. Jia, Q. Liu, L. Zhang, C. Du, J. Chen, H. Ye, X. Li, Y. Li, T. Shen, Y. Tang, J. Huang, *Angew. Chem., Int. Ed.* **2018**, *130*, 12932.
[26] B. Xiang, L. Wang, G. Liu, A. M. Minor, *J. Electrochem. Soc.* **2013**, *160*, A415.
[27] Z. Wang, Y. Fu, Z. Zhang, S. Yuan, K. Amine, V. Battaglia, G. Liu, *J. Power Sources* **2014**, *260*, 57.
[28] A. C. Kozen, C.-F. Lin, A. J. Pearse, M. A. Schroeder, X. Han, L. Hu, S.-B. Lee, G. W. Rubloff, M. Noked, *ACS Nano* **2015**, *9*, 5884.
[29] J. Zhao, Z. Lu, N. Liu, H.-W. Lee, M. T. McDowell, Y. Cui, *Nat. Commun.* **2014**, *5*, 5088.
[30] J. Zhao, Z. Lu, H. Wang, W. Liu, H.-W. Lee, K. Yan, D. Zhuo, D. Lin, N. Liu, Y. Cui, *J. Am. Chem. Soc.* **2015**, *137*, 8372.
[31] T. Kang, Y. Wang, F. Guo, C. Liu, J. Zhao, J. Yang, H. Lin, Y. Qiu, Y. Shen, W. Lu, L. Chen, *ACS Cent. Sci.* **2019**, *5*, 468.
[32] J. Zhao, G. M. Zhou, K. Yan, J. Xie, Y. Z. Li, L. Liao, Y. Jin, K. Liu, P. C. Hsu, J. Y. Wang, H. M. Cheng, Y. Cui, *Nat. Nanotechnol.* **2017**, *12*, 993.
[33] Y. Zhao, K. Zheng, X. Sun, *Joule* **2018**, *2*, 2583.
[34] Z. Tu, S. Choudhury, M. J. Zachman, S. Wei, K. Zhang, L. F. Kourkoutis, L. A. Archer, *Nat. Energy* **2018**, *3*, 310.
[35] J. Liang, X. Li, Y. Zhao, L. V. Goncharova, G. Wang, K. R. Adair, C. Wang, R. Li, Y. Zhu, Y. Qian, *Adv. Mater.* **2018**, *30*, 1804684.
[36] Q. Pang, X. Liang, A. Shyamsunder, L. F. Nazar, *Joule* **2017**, *1*, 871.
[37] D. Foix, D. Gonbeau, G. Taillades, A. Pradel, M. Ribes, *Solid State Sci.* **2001**, *3*, 235.
[38] A. Haas, *Angew. Chem., Int. Ed. Engl.* **1965**, *4*, 1014.
[39] S. Jeong, D. Bresser, D. Buchholz, M. Winter, S. Passerini, *J. Power Sources* **2013**, *235*, 220.
[40] C. Wang, X. Li, Y. Zhao, M. N. Banis, J. Liang, X. Li, Y. Sun, K. R. Adair, Q. Sun, Y. Liu, F. Zhao, S. Deng, X. Lin, R. Li, Y. Hu, T.-K. Sham, H. Huang, L. Zhang, R. Yang, S. Lu, X. Sun, *Small Methods* **2019**, 1900261, https://doi.org/10.1002/smtd.201900261.